Open Research Online

HST F160W Imaging of Very Massive Galaxies at 1.5 <z <3.0: Diversity of Structures and the Effect of Close Pairs on Number Density Estimates

Journal Item

For guidance on citations see FAQs.
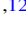
oro.open.ac.uk

HST F160W Imaging of Very Massive Galaxies at $1.5 < z < 3.0$: Diversity of Structures and the Effect of Close Pairs on Number Density Estimates

Z. Cemile Marsan[1,15] , Danilo Marchesini[2] , Adam Muzzin[1] , Gabriel B. Brammer[3,4] , Rachel Bezanson[5] , Marijn Franx[6] , Ivo Labbé[7], Britt Lundgren[8] , Gregory Rudnick[9] , Mauro Stefanon[6] , Pieter van Dokkum[10] , David Wake[11,12] , and Katherine E. Whitaker[13,14]

[1] Department of Physics and Astronomy, York University, 4700 Keele Street, Toronto, Ontario, MJ3 1P3, Canada; cmarsan@yorku.ca
[2] Department of Physics and Astronomy, Tufts University, 574 Boston Avenue, Medford, MA 02155, USA
[3] Space Telescope Science Institute, 3700 San Martin Drive, Baltimore, MD 21218, USA
[4] Cosmic Dawn Center, Niels Bohr Institute, University of Copenhagen, Juliane Maries Vej 30, DK-2100 Copenhagen Ø, Denmark
[5] Department of Physics and Astronomy and PITT PACC, University of Pittsburgh, Pittsburgh, PA 15260, USA
[6] Leiden Observatory, Leiden University, P.O. Box 9513, 2300 RA Leiden, The Netherlands
[7] Centre for Astrophysics and Supercomputing, Swinburne University of Technology, Hawthorn, VIC 3122, Australia
[8] Department of Physics, University of North Carolina Asheville, One University Heights, Asheville, NC 28804, USA
[9] Department of Physics and Astronomy, The University of Kansas, 1251 Wescoe Hall Drive, Lawrence, KS 66045, USA
[10] Department of Astronomy, Yale University, New Haven, CT 06511, USA
[11] Department of Physics, University of North Carolina Asheville, One University Heights, Asheville, NC 28804, USA
[12] Department of Physical Sciences, The Open University, Milton Keynes MK7 6AA, UK
[13] Department of Physics, University of Connecticut, Storrs, CT 06269, USA
[14] Cosmic Dawn Center (DAWN), Niels Bohr Institute, University of Copenhagen/DTU-Space, Technical University of Denmark

Abstract

We present a targeted follow-up *Hubble Space Telescope* WFC3 F160W imaging study of very massive galaxies ($\log(M_{star}/M_\odot) > 11.25$) selected from a combination of ground-based near-infrared galaxy surveys (UltraVISTA, NEWFIRM Medium Band Survey-II , UKIRT Infrared Deep Sky Survey (UKIDSS) Ultra-Deep Survey (UDS) at $1.5 < z < 3$). We find that these galaxies are diverse in their structures, with $\sim 1/3$ of the targets being composed of close pairs, and span a wide range in sizes. At $1.5 < z < 2.5$, the sizes of both star-forming and quiescent galaxies are consistent with the extrapolation of the stellar mass–size relations determined at lower stellar masses. At $2.5 < z < 3.0$, however, we find evidence that quiescent galaxies are systematically larger than expected based on the extrapolation of the relation derived using lower stellar mass galaxies. We used the observed light profiles of the blended systems to decompose their stellar masses and investigate the effect of the close pairs on the measured number densities of very massive galaxies in the early universe. We estimate correction factors to account for close-pair blends and apply them to the observed stellar mass functions (SMFs) measured using ground-based surveys. Given the large uncertainties associated with this extreme population of galaxies, there is currently little tension between the (blending-corrected) number density estimates and predictions from theoretical models. Although we currently lack the statistics to robustly correct for close-pair blends, we show that this is a systematic effect that can reduce the observed number density of very massive galaxies by up to a factor of ~ 1.5, and should be accounted for in future studies of SMFs.

Key words: galaxies: high-redshift – galaxies: structure – infrared: galaxies

1. Introduction

In contrast to the hierarchical assembly of dark matter halos, observations indicate that the most massive galaxies in the nearby universe were among the first to build-up their stellar mass and quench. In the nearby universe, massive galaxies are found to be older, more metal-rich, and to have formed their stars more rapidly and at earlier cosmic epochs compared to their lower-mass counterparts (Trager et al. 2000; Terlevich et al. 2001; Bernardi et al. 2003; Gallazzi et al. 2005, 2006; Thomas et al. 2005; Yamada et al. 2006; Kuntschner et al. 2010; McDermid et al. 2015). Corroborating their early formation times are results from recent deep near-infrared (NIR) surveys, which reveal that very massive galaxies were already in place by $z \sim 4$ (merely ~ 1.5 Gyr after the Big Bang; e.g., Marchesini et al. 2010; Ilbert et al. 2013; Muzzin et al. 2013b; Duncan et al. 2014; Straatman et al. 2014; Tomczak et al. 2014; Caputi et al. 2015; Grazian et al. 2015; Song et al. 2016; Davidzon et al. 2017), and spectroscopic follow-up

campaigns, confirming that these massive galaxies have evolved stellar populations at $z > 3$ (e.g., Marsan et al. 2015, 2017; Glazebrook et al. 2017; Schreiber et al. 2018). Thus, the observed properties of the most massive galaxies serve as critical benchmarks to understand the detailed physical mechanisms that impact galaxy formation and evolution in the early universe.

A two-phase scenario has been proposed for the evolution of massive galaxies: a rapid, compact formation at early epochs via highly dissipative processes (e.g., by experiencing gas-rich major mergers or violent disk instabilities; Hopkins et al. 2006; Dekel et al. 2009; Krumholz & Burkert 2010; Dekel & Burkert 2014; Wellons et al. 2015; Bournaud 2016), and following the quenching of star formation, a later phase of assembly dominated by undergoing dry minor mergers with satellite galaxies (Nipoti et al. 2003; Khochfar & Silk 2006; Naab et al. 2009; Oser et al. 2010; Hilz et al. 2012, 2013). Several observables serve to corroborate this scenario: the uniform, old stellar populations of $z \sim 0$ massive galaxies (McDermid et al. 2015), the build-up of stellar halos in (central) massive galaxies (e.g., Buitrago et al. 2017; Huang et al. 2018b, 2018a), and the dramatic size

---
[15] York Science Fellow.

evolution observed for the massive, quiescent galaxy population since $z \sim 2$ (Trujillo et al. 2006; Buitrago et al. 2008; Cimatti et al. 2008; Franx et al. 2008; van Dokkum et al. 2008; Bezanson et al. 2009; Damjanov et al. 2009; Kriek et al. 2009a; van Dokkum et al. 2010; Williams et al. 2010; van der Wel et al. 2011, 2014; Newman et al. 2012; Szomoru et al. 2012; Whitaker et al. 2012; Patel et al. 2013; Belli et al. 2014, 2015; Faisst et al. 2017; Hill et al. 2017).

The structural evolution of galaxies is sensitive to their assembly history and feedback processes, as such, the observed size and morphology of galaxies in various environment and halo mass regimes is a critical benchmark for theoretical models to reproduce (e.g., Furlong et al. 2017; Genel et al. 2018). A census of galaxy size has now been obtained out to $z \sim 4$ across a wide range in stellar mass and star formation activity (e.g., Shen et al. 2003; Trujillo et al. 2004; Bezanson et al. 2009; Patel et al. 2013; van der Wel et al. 2014; van Dokkum et al. 2014; Straatman et al. 2015; Allen et al. 2017). However, the majority of information on the size evolution of massive galaxies is obtained from samples with stellar masses in the range of $1-2 \times 10^{11} M_{\odot}$; as such, the size–mass relation at the extreme massive end of the galaxy population (i.e., $\log(M_*/M_{\odot}) \geqslant 11.25$) at $z > 1.5$ remains poorly constrained. Abundance matching techniques suggest that ultra-massive galaxies, those with $\log(M_*/M_{\odot}) > 11.25$ should reside in dark matter halos of a few $\times 10^{14} M_{\odot}$ at all redshifts, implying that they are the progenitors of the Brightest Cluster Galaxies in the local universe. Therefore, measuring how these massive systems evolve in size compared to their (relatively) lower-mass cousins could provide valuable information on how their assembly takes place, and whether this evolution is related to their halo properties (e.g., concentration, mass, or subhalo occupation number).

Owing to the low spatial density of these objects, identifying a statistically large sample of very massive galaxies requires relatively deep and wide NIR surveys using ground-based facilities, which typically lack the spatial resolution to derive robust sizes for these compact, distant galaxies (the typical FWHM $\sim 0''.8-1''$ corresponds to a physical size of $\sim 6-9$ kpc at $z = 1.5-3$). To this end, we have obtained follow-up HST/WFC3 H_{160} imaging for a sample of very massive ($\log(M_*/M_{\odot}) > 11.25$) galaxies at $1.5 < z < 3.0$ selected using relatively deep and wide-field ground-based NIR surveys. The H_{160} band, the reddest filter currently available for high-resolution imaging, probes the rest-frame wavelength regime just blueward of the r band (~ 6100 Å) at $z \sim 1.5$ to wavelengths just redward of the rest-frame Balmer break at $z \sim 3.0$ (i.e., ~ 3900 Å).

In this study, we present the HST/WFC3 H_{160} imaging for 37 targets with stellar masses $\log(M_*/M_{\odot}) > 11.25$ at $1.5 < z < 3.0$ in the NEWFIRM Medium Band Survey-II (NMBS-II), UltraVISTA and UKIRT Infrared Deep Sky Survey (UKIDSS) Ultra-Deep Survey (UDS). In Section 2 we briefly describe the data sets used to select this sample and the targeted HST observations. Section 3 presents the analysis and relevant measurements employed in this study. We present the results in Section 4 and summarize these results in Section 5. Throughout this paper we assume the standard ΛCDM cosmological parameters $\Omega_M = 0.3$, $\Omega_\Lambda = 0.7$ with $H_0 = 70$ km s^{-1} Mpc^{-1} and a Chabrier (2003) initial mass function. All magnitudes listed are in the AB system.
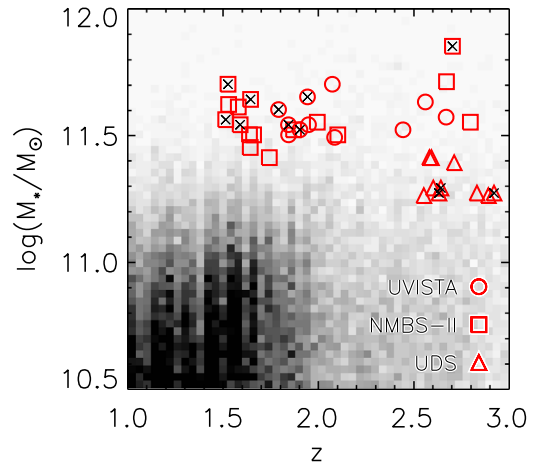

Figure 1. Distribution of stellar masses as a function of redshift for the sample of very massive galaxies at $1.5 < z < 3.0$ targeted with HST WFC3 H_{160} band imaging (open red symbols). Targets selected from the UltraVISTA D1, NMBS-II, and UDS DR8 catalogs are represented as circles, squares, and triangles, respectively. Targets that are discovered to be close pairs are marked with X. The grayscale represents the distribution of galaxies above the magnitude completeness limit of each parent photometric galaxy survey.

2. Data

2.1. Parent Catalogs

We use the NMBS-II (Annunziatella et al. 2018) and the UltraVISTA survey (Muzzin et al. 2013b) to identify and select the rare, very massive ($\log(M_*/M_{\odot}) > 11.25$) galaxies at $1.5 < z < 3.0$ for targeted follow-up HST WFC3/H_{160} imaging (GO12990, PI: Muzzin).

We also utilize the HST H_{160} imaging follow-up study of $\log(M_*/M_{\odot}) > 11.25$ quiescent galaxies at $2.5 < z < 3.0$ (GO13002, PI: Williams) selected from the UKIDSS UDS (Lawrence et al. 2007) to extend our sample to include massive, quiescent galaxies. These surveys combine to an effective area of ~ 5.9 deg^2. Below, we briefly describe the photometric catalogs and the spectral energy distribution (SED) fitting, and refer the reader to the works mentioned for further details related to data processing, photometry, and SED modeling assumptions.

The NMBS-II is a wide, but relatively shallow NIR ($K = 21.75$, 5σ) survey, covering a total area of ~ 4.25 deg^2 in the CFHTLS-D1, CFHTLS-D4, COSMOS, and MUSYC fields. This survey combines deep NIR medium-bandwidth photometry (J_1, J_2, J_3, H_1, H_2) with the existing UV, optical, and NIR data in these fields to accurately identify evolved, massive galaxies by tracing the rest-frame optical break (~ 4000 Å) at $z > 1$. In the COSMOS field (Scoville et al. 2007), where the NMBS-II footprint overlaps with the UltraVISTA survey (~ 1.62 deg^2, $K = 23.8$, McCracken et al. 2012) we used the K_S-selected galaxy catalog from Muzzin et al. (2013b) to complement the wider-field, yet shallower, NMBS-II data set. Photometric redshifts are estimated using EAZY (Brammer et al. 2008) and the stellar population parameters, including stellar mass, are calculated using FAST (Kriek et al. 2009b) assuming exponentially declining star formation histories, fixed solar metallicity, and the Calzetti et al. (2000) dust reddening law.

Targets in the UDS field are selected from the photometric catalog presented in Williams et al. (2009, 2010) and Quadri et al. (2012) using Data Release 8 of the UKIDSS NIR imaging
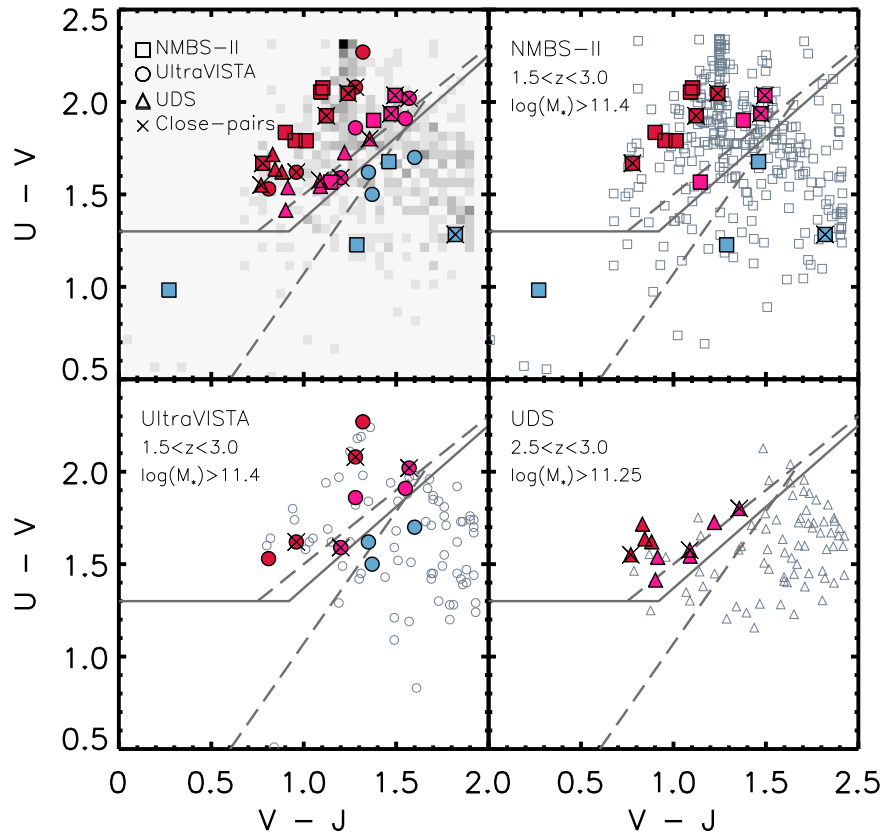
Figure 2. Rest-frame $U–V$ vs. $V–J$ color–color diagram. The filled symbols indicate the rest-frame colors for the $1.5 < z < 3.0$ galaxies with targeted *HST* observations. Targets that are discovered to be close pairs are marked with an X. The cuts used to separate star-forming (blue) from quiescent (red and pink) galaxies from van der Wel et al. (2014) are shown with solid gray lines. Also shown, with dashed lines, is the separation between quiescent, unobscured and dusty star-forming galaxies from Martis et al. (2016). Top left panel displays the colors for the targeted *HST* sample, along with all sources that satisfy the sample selection criteria in each photometric galaxy catalog (grayscale). Top right and bottom panels focus on the individual parent photometric galaxy catalogs and display the colors for all sources that satisfy the redshift and stellar mass criteria adopted (indicated in legend).

(reaching 5σ point-source depth of $K = 24.5$) over an effective area of ~ 0.62 deg^2. This data set also includes u', B, V, R, i', z', J, H, and *Spitzer* IRAC 3.6 and 4.5 μm band photometry. Photometric redshifts, stellar masses, and other stellar population parameters were estimated in an identical manner as described above for the NMBS-II and UltraVISTA photometric catalog papers.

2.2. Targeted Sample for HST WFC3 H_{160} Imaging

The point-spread function (PSF) of typical ground-based near-IR imaging is insufficient to reliably measure sizes of the smallest galaxies at $z > 1$ (where FWHM $\sim 0.''8$ corresponds to physical distances of ~ 6–7 kpc at $1 < z < 3$). We therefore utilized follow-up *HST* imaging in the reddest WFC3 band, H_{160}, to obtain size measurements of our targets.

Figure 1 highlights that the galaxies in this sample are among the most massive ones at the epochs probed. The grayscale representation shows all galaxies brighter than the magnitude limit of each parent catalog (UDS DR8: $K = 24$; UltraVISTA DR1: $K = 23.8$; NMBS-II: $K = 21.75$), with red symbols denoting the follow-up targets. From the combined UltraVISTA DR1 and NMBS-II photometric catalogs, a total of 27 targets at $1.5 < z < 3$ with robust stellar mass estimates $\log(M_*/M_\odot) > 11.25$ were selected for *HST*/WFC3 follow-up observations (GO12990, PI: Muzzin); represented with open circles and squares, respectively, in Figure 1. The open triangles represent the additional 10 quiescent galaxies with

$\log(M_*/M_\odot) > 11.25$ at $2.5 < z < 3.0$ that were selected for *HST*/WFC3 follow-up observations in the UDS field (GO13002, PI: Williams; see Patel et al. 2017). The combination of these data sets yields a total of 37 galaxies at $1.5 < z < 3$ with $\log(M_*/M_\odot) > 11.25$, increasing the available high-resolution imaging for this extreme population by a factor of ~ 2 compared to the CANDELS data set for galaxies with $\log(M_*/M_\odot) > 11.4$ (van der Wel et al. 2014).

Figure 2 shows the rest-frame $U–V$ versus $V–J$ color diagram, frequently used to distinguish star-forming and quiescent galaxies (e.g., Labbé et al. 2005; Whitaker et al. 2011; Muzzin et al. 2013a). The rest-frame colors were calculated using EAZY (Brammer et al. 2008). For consistency with van der Wel et al. (2014), we used the updated rest-frame color cuts of Williams et al. (2009) to separate star-forming (blue symbols) from quiescent galaxies (red and pink symbols). Based on their rest-frame colors, 30 ($\sim 80\%$ of total) very massive galaxies at $1.5 < z < 3$ fall into the quiescent region. Compared to the quiescent fractions derived by Martis et al. (2016) using a combination of the UltraVISTA DR1 and CANDELS data sets, our sample is characterized by a larger quiescent fraction, although the estimated quiescent fraction in the largest stellar mass bin ($11.5 < \log(M_*/M_\odot) < 11.8$) in Martis et al. (2016) is very uncertain. Noticing that a significant portion of our targets lie close to the *UVJ* selection cuts, we calculated a quiescent fraction to account for contamination from potential post-starburst or fading galaxies with intermediate colors (pink
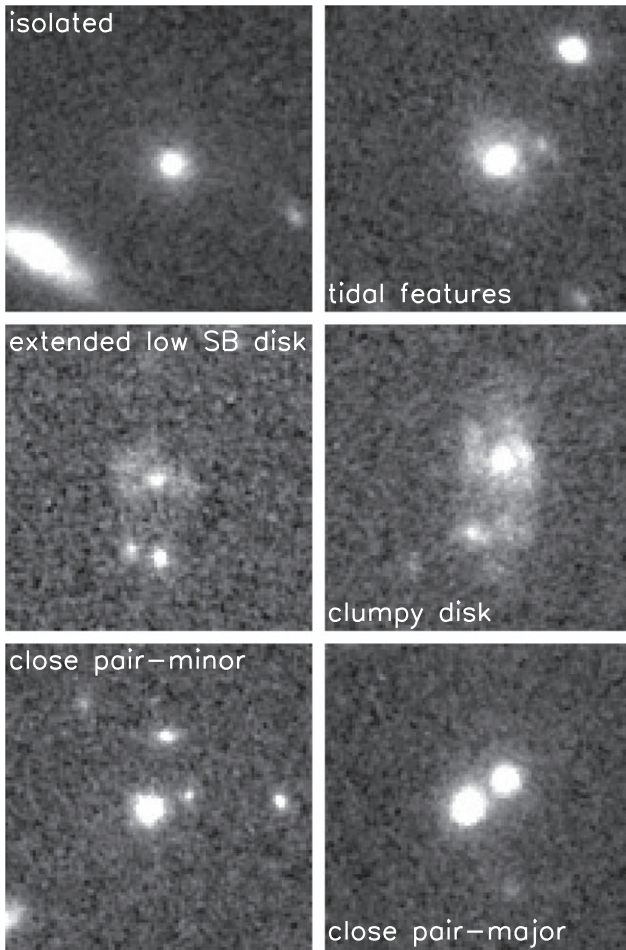
Figure 3. H_{160} stamps of targets displaying the structural diversity of the sample of very massive galaxies at $1.5 < z < 3.0$. Size of each image stamp is $6'' \times 6''$.

symbols in Figure 2). Selecting galaxies that are > 0.2 mag away from the diagonal color cut (red symbols in Figure 2), we calculated a conservative quiescent fraction of $\sim 45\%$. The few star-forming galaxies tend to have colors consistent with accumulating along the quiescent-star-forming transition zone at the dusty end of the star-forming region, with only one relatively unobscured star-forming galaxy.

3. Analysis

Visually investigating the H_{160} images of the 37 targets in this study reveals that very massive galaxies at $1.5 < z < 3.0$ are morphologically diverse, in contrast to their local universe counterparts. Figure 3 displays examples for the variety of structures observed: an isolated and morphologically undisturbed galaxy, a target with faint tidal features, a galaxy exhibiting the presence of an extended low-surface brightness disk, a galaxy displaying prominent features of disturbance and close-pair systems. Interestingly, 13 targets ($\sim$one-third of the total sample) are found to be composed of multiple objects that are not resolved in the ground-based images (indicated with red stars in the corresponding H_{160} panels of Figures 4–6). We further explore this effect of source multiplicity on the high-mass end of the galaxy stellar mass function (SMF) at $1.5 < z < 3$ inferred from ground-based NIR galaxy surveys in Section 4.2.

3.1. Modeling 2D Light Profiles

The *HST* H_{160} data were reduced with AstroDrizzle in a similar manner as CANDELS imaging (Koekemoer et al. 2011). The exposures from the four-point dither pattern were combined to a final pixel scale of $0.''06$. The total exposure time for each target ranged from ~ 500–2400 s.

We used GALFIT (Peng et al. 2002) to model the two-dimensional light profiles and to obtain the structural parameters for the $\log(M_*/M_\odot) > 11.25$ sample of galaxies at $1.5 < z < 3$ using cutouts of size $12'' \times 12''$ centered around each target's position.

An empirical PSF to be included in GALFIT modeling was created for each target by median-stacking the sky-subtracted, two-dimensional light profiles of bright, unsaturated stars located within its frame. The *HST* imaging resolution (FWHM $\approx 0.''18$) is a factor of ≈ 4–5 greater compared to the seeing of the ground-based NIR observations ($\sim 0.''8$). When extended, bright objects were present in image stamps, we created a bad pixel map to mask out these components when fitting with GALFIT. Following van der Wel et al. (2014) and others, the sky background level was kept fixed in the fitting procedure, which we estimated as the mode of sky pixel values after masking out all objects in the image stamps. We also repeated this analysis by allowing GALFIT to fit for the sky background, finding that the results were quantitatively robust against the specific treatment for the sky background. We constructed uncertainty maps to be used as inputs for GALFIT by adding the Poisson noise across the images and the noise calculated from the inverse variance maps produced by AstroDrizzle (corresponding to the instrumental noise) in quadrature.

A single-component Sérsic model was used to model the light profiles of the targets simultaneously with all other objects located within their H_{160} stamps. Specifically, we used GALFIT to determine the best-fit total magnitude (H_{160}), half-light radius along the semimajor axis ($r_{1/2,\mathrm{maj}}$), Sérsic index (n), axis ratio (b/a), position angle, and the centroid for each object. A constraint file was created to force GALFIT to restrict the fit Sérsic indices between $n = 0.25$–8, the semimajor half-light radii between 1–50 pixels (50 pixels $= 3''$, corresponding to ~ 23–25 kpc at $z \approx 1$–3) and the total magnitudes of sources within ± 3 mag of the parent catalog H band photometry. When the radius along the semimajor axis reached the extreme value of $r_{1/2,\mathrm{maj}} = 50$ pixels, we reran GALFIT after relaxing the upper constraint to $r_{1/2,\mathrm{maj}} = 100$ pixels.

We initially modeled the observed light profiles multiple times for each target by varying initial guesses to obtain a measure of the dependence of the best-fit Sérsic parameters on GALFIT inputs. Specifically, we ran GALFIT 100 times for each target by selecting the initial input values for the effective radius and n from a random distribution of values between 1–20 pixels and 1–6, respectively. When estimating confidence limits, we only considered the GALFIT models that yielded valid results, discarding models that did not converge numerically. The confidence limit for each structural parameter was determined by using the 1σ standard deviation of its distribution (i.e., by integrating the probability distribution of each parameter from the extremes until the integrated probability is equal to $0.3173/2 = 0.1586$).

As galaxies are more compact at high-z, we additionally investigated the effect of PSF model choice on the estimated structural parameters by running GALFIT on each target using all the empirical PSFs (36 additional for each target). The final
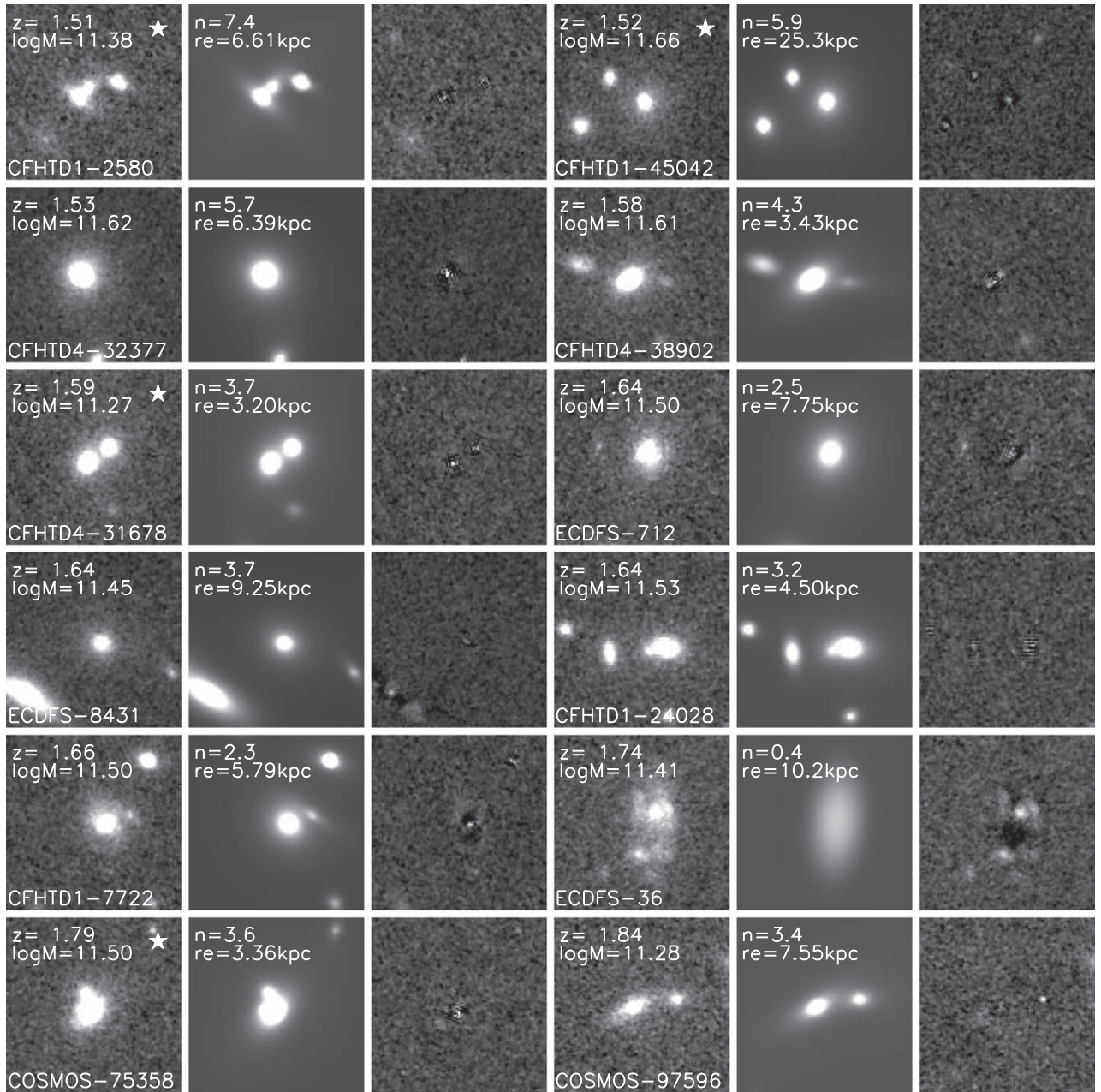
Figure 4. The variety of the 2D light profiles of the $1.5 < z < 3.0$ massive galaxies. The *HST* H_{160} image cutouts (panels with target name, redshift, and stellar mass in legend), best-fit 2D light profile (panels with n and R_e indicated) and the residual image is displayed for each target. Panels with white stars indicate targets that are resolved as multiple components in the *HST* H_{160} imaging. Panels are 6″ on each side.

1σ confidence limits were then calculated by combining the scatter of Sérsic parameters derived in this manner with the former 1σ distribution values in quadrature.

Table 1 lists the photometric redshifts, and the photometrically derived stellar masses (after the decomposing for the blended sources, indicated with *; see Section 3.2) of the targeted sample, along with their best-fit GALFIT structural properties and corresponding 1σ uncertainties.

Figures 4–6 show the GALFIT-modeled H_{160} stamps, along with the best-fit GALFIT 2D models and the residuals (displayed using identical scaling in the panels for each target). The legend of the direct H_{160} imaging panels lists the target ID, $z_{\rm phot}$, and stellar mass, whereas the best-fit structural parameters are listed in the legends of the GALFIT model panels. Panels

with red stars indicate the targets that are revealed to be multiple sources in the H_{160} imaging.

3.2. Stellar Mass Decomposition of HST Resolved Close Galaxy Pairs

In this section we focus on the targets that are resolved as multicomponent systems in H_{160} imaging. We used the observed H_{160} magnitudes of close galaxy pairs (centrals and companions) as proxies to decompose the stellar masses of ground-based blended objects. While this method is not ideal, we will show that it is an appropriate first-order approximation to assume that the central and companion galaxies have stellar masses proportional to their light observed in the H_{160} band. In
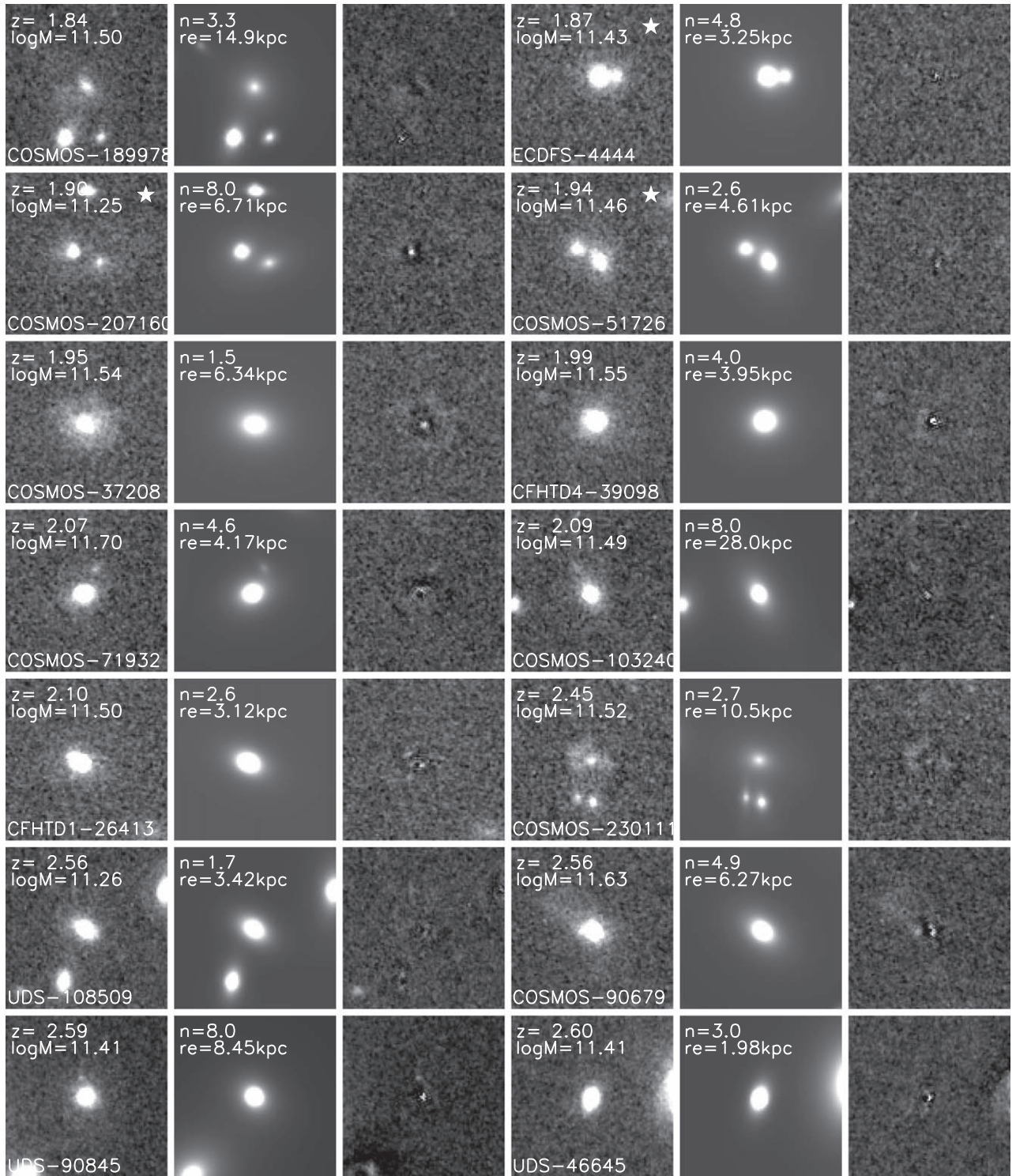
Figure 5. See caption of Figure 4.

other words, we assume identical mass to light ratios (M_*/L_H) for the *HST* resolved components and use their observed H_{160} band fluxes as direct tracers for their underlying stellar masses. This inherently brings with it two additional assumptions for the properties of *HST* resolved close pairs: (1) that the close pairs are physically associated—i.e., not chance superpositions of objects at different redshifts along the line of sight, and (2) that the central and companion galaxies have similar stellar populations. Strict proof for the validity of these assumptions

requires spectroscopic redshift identifications of the resolved components, and multiwavelength, space-based imaging of all targeted objects, which are currently not available.

To address the first assumption, we checked the publicly available spectroscopic catalogs for these widely studied fields (VIMOS Ultra Deep Survey, Le Fèvre et al. 2015; Tasca et al. 2017; zCOSMOS, Lilly et al. 2007; DEIMOS 10k spectroscopic catalog of the COSMOS field, Hasinger et al. 2018; VANDELS spectroscopic survey of the UDS and CDFS fields,

Figure 6. See caption of Figure 4.

McLure et al. 2018), finding no matches. Only one of the targets (COSMOS-207160—that has two resolved component centers located ∼1″1 apart) was id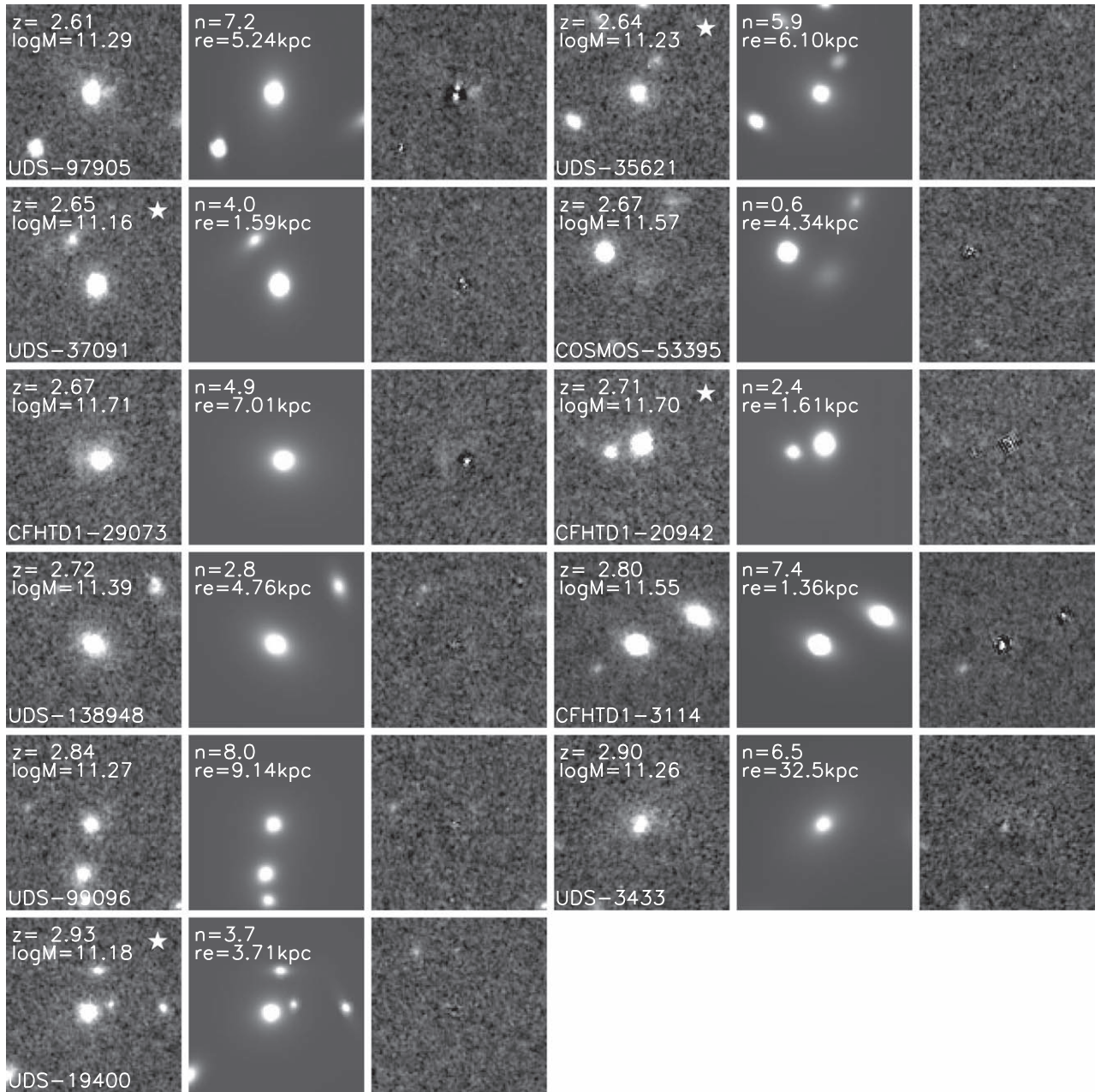entified in the grism redshift catalog of 3D-*HST* (Momcheva et al. 2016). This target has a $z_{peak} = 1.91^{+0.13}_{-0.11}$ in the parent catalog from which it was selected (UVISTA). The z_{grism} in the 3D-*HST* redshift catalog for the resolved sources are $2.05^{+0.01}_{-0.02}$ and $2.36^{+0.0001}_{-0.02}$. There are no discernible color differences between the two resolved sources. Although the true physical pairs cannot be identified without spectroscopic redshifts, at such small angular scales, it is more likely that the pairs are physically associated rather than chance aligned (Quadri et al. 2012).

In order to investigate the validity of the second assumption, i.e., that the M_*/L_H of close pairs are similar, we utilized the publicly available deep *HST* ACS/F814W band (hereafter, i_{814}) imaging of the COSMOS field to investigate the color differences between resolved sources, as a proxy of different stellar populations. Figure 7 shows the $i_{814}+H_{160}$ color composite images for the four targets with available i_{814} imaging. Visually, there are no discernible differences between the colors of resolved objects, supporting the scenario that they do not have significantly different stellar populations. To quantitatively assess the color differences of the *HST* resolved components, we calculated the i_{814} and H_{160} magnitudes using a circularized aperture of $d = 0″3$ centered at their locations. Not surprisingly, due to the faintness of these targets just below $\lambda_{obs} \sim 1\mu m$ (see Appendix), they are barely detected/resolved in i_{814} imaging at best, and therefore their calculated magnitudes have significant uncertainties associated with them due to Poisson statistics (the uncertainty in the calculated color differences is dominated by this term). We estimated the noise due to variations in the sky background by calculating the σ of
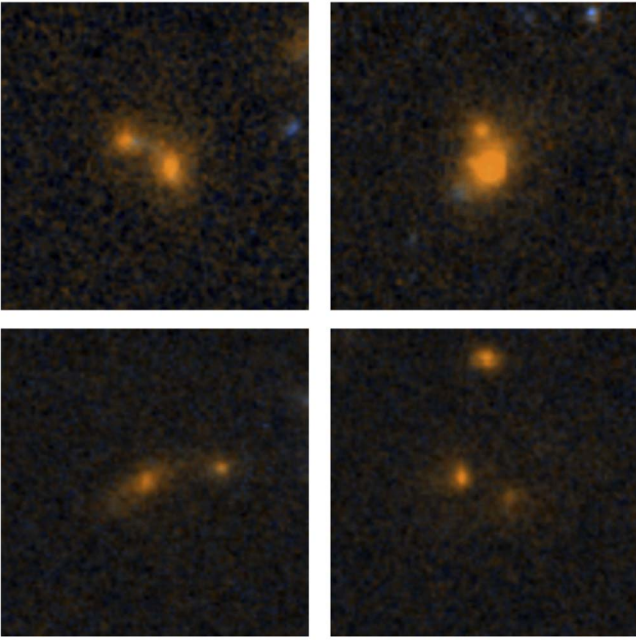
Figure 7. Color images for the four targets in our sample located in the COSMOS field that have publicly available ACS imaging.
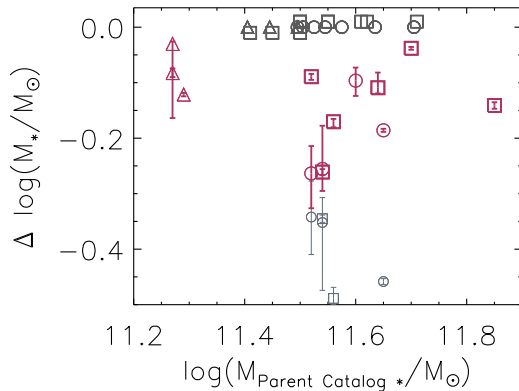

Figure 8. Difference in stellar mass estimates once blending due to close pairs has been accounted for. The brighter, more massive component of the blended targets is plotted in red, whereas the companions, i.e., the lower mass components are plotted in light gray. The stellar masses of the targets identified as being composed of close pairs are calculated by scaling the parent catalog stellar mass by the relative fluxes of the resolved components (see Section 3.2). Targets selected from UltraVISTA, NMBS-II, and UDS catalogs are represented as circles, squares, and triangles.

the Gaussian fit to the distribution of fluxes measured in $d = 0\farcs3$ apertures on empty regions of the sky, and added this value in quadrature to the uncertainty on the measured i_{814} magnitudes. The color differences between resolved close pairs range from $\Delta(i_{814} - H_{160}) = 0.3$–2.3 mag; however, the colors of pairs are all consistent with each other within 1σ uncertainties.

In addition to investigating the size–stellar mass relation at its extreme massive end, we are seeking to constrain the effect of blending in ground-based surveys on the inferred number density of very massive galaxies at $z > 1.5$. Assuming similar M_*/L_H ratios for the blended objects translates to constraining the maximum allowed change due to blending on the extreme massive end of the SMF at $z > 1.5$. In fact, even if there are color differences that we are not able to discern, the assumption

that resolved close pairs have identical M_*/L_H ratios *maximally* reduces the stellar mass of the central (brighter, and hence more massive) galaxy. If the fainter companions have younger stellar populations, it is expected that $(M_*/L_H)_{\rm companion} < (M_*/L_H)_{\rm central}$, which would work to decrease the stellar mass allocated to the companion. Hence, assuming identical M_*/L_H ratios for *HST* resolved close pairs of galaxies sets a conservative lower limit to the stellar mass of the central galaxies.

Figure 8 serves to illustrate the effect of decomposing the stellar masses of resolved targets using this approach. The decomposed masses of K band blended targets are shown with red and light gray symbols. The error bars on the deblended masses of close pairs are calculated using the 1σ standard deviation of their distribution in H_{160} magnitude differences (i.e., $H_{160,\rm central} - H_{160,\rm companion}$). We caution that the stellar masses inferred for the less bright companions should not be taken at face value; rather, they are plotted in this figure to guide the eye to reflect the extent of blending. The median (mean) difference in the inferred stellar mass of the main/ central galaxies is $\Delta \log(M_*) \sim 0.12(0.14)$ dex. The difference in stellar mass inferred for the most major blends is $\Delta \log(M_*) \approx 0.25$ dex.

4. Results

4.1. The Size–Mass Relation

We used the radius along the semimajor axis of the half-light ellipse ($r_{1/2,\rm maj}$) as a proxy for the sizes of our targets, rather than the often-calculated circularized effective radius in order to compare our results directly with van der Wel et al. (2014). We converted the sizes of the modeled galaxies to the rest-frame 5000 Å, using Equations 1 and 2 in van der Wel et al. (2014) to correct for stellar mass and redshift dependent color gradients. Table 1 lists all sizes standardized to the rest-frame $\lambda = 5000$Å.

Figure 9 shows our targeted sample of very massive galaxies at $1.5 < z < 3.0$ in the size–stellar mass diagram, along with the measurements from van der Wel et al. (2014). The top panels show the size measurements for individual galaxies. The small red and blue points indicate the quiescent and star-forming galaxies from the CANDELS sample from van der Wel et al. (2014) at the targeted redshifts. Filled orange and cyan symbols represent our targeted sample of quiescent and star-forming galaxies, respectively. The filled circles indicate targets resolved both in the K and H_{160} bands (larger filled circles), or the central/main galaxies in blends (smaller filled circles). The square symbols represent the fainter companion galaxies with inferred deblended stellar mass $\log(M_*/M_\odot) > 11.0$. We note the large range in sizes observed at the extreme massive end probed by this sample. With this targeted *HST* sample, the number of galaxies with robust size determinations increases by a factor of ~ 2 in the lowest redshift bin, $1.5 < z < 2.0$, for both quiescent and star-forming galaxies with $\log(M_*/M_\odot) > 11.4$. Additionally, where the van der Wel et al. (2014) sample has only a single $\log(M_*/M_\odot) > 11.4$ (11.2) quiescent galaxy at $2.0 < z < 2.5$ ($2.5 < z < 3.0$), this sample adds crucial observations where CANDELS cannot probe due to its relatively narrow effective area.

The bottom panels of Figure 9 display the biweighted mean sizes inferred for massive $1.5 < z < 3.0$ galaxies. The size–stellar mass relations from van der Wel et al. (2014, red and

Table 1
Best-fit GALFIT Structural Parameters

Target	R.A. (h:m:s)	Decl. (d:m:s)	z	$\log(M_*/M_\odot)$ (dex)	R_e (kpc)	n	b/a
CFHTD1-2580*	02: 24: 42.279	−04: 53: 34.98	$1.51^{+0.07}_{-0.07}$	11.38	$6.61^{+1.20}_{-1.48}$	$7.42^{+0.54}_{-0.77}$	$0.32^{+0.02}_{-0.02}$
CFHTD1-45042*	02: 24: 19.551	−04: 08: 27.76	$1.52^{+0.07}_{-0.07}$	11.66	$25.40^{+0.00}_{-0.00}$	$5.94^{+0.22}_{-0.21}$	$0.66^{+0.21}_{-0.05}$
CFHTD4-32377	22: 15: 57.971	−17: 40: 20.48	1.465^a	11.60	$6.39^{+0.60}_{-0.60}$	$5.72^{+0.68}_{-0.68}$	$0.93^{+0.01}_{-0.01}$
CFHTD4-38902	22: 15: 56.557	−17: 26: 55.81	$1.58^{+0.11}_{-0.09}$	11.61	$3.42^{+1.02}_{-0.60}$	$4.29^{+1.35}_{-1.03}$	$0.59^{+0.02}_{-0.02}$
CFHTD4-31678*	22: 15: 44.443	−17: 41: 50.14	$1.59^{+0.08}_{-0.08}$	11.27	$3.21^{+0.08}_{-0.08}$	$3.78^{+0.33}_{-0.33}$	$0.91^{+0.12}_{-0.03}$
ECDFS-712	03: 31: 46.077	−28: 00: 26.48	$1.64^{+0.10}_{-0.10}$	11.50	$7.76^{+0.07}_{-0.07}$	$2.58^{+0.08}_{-0.08}$	$0.82^{+0.00}_{-0.00}$
ECDFS-8431	03: 32: 42.636	−27: 38: 15.93	$1.64^{+0.08}_{-0.09}$	11.45	$9.26^{+0.39}_{-0.39}$	$3.77^{+0.22}_{-0.22}$	$0.85^{+0.01}_{-0.01}$
CFHTD1-24028*	02: 27: 09.848	−04: 44: 53.99	$1.64^{+0.12}_{-0.11}$	11.53	$4.50^{+0.17}_{-0.17}$	$3.26^{+0.31}_{-0.31}$	$0.65^{+0.04}_{-0.04}$
CFHTD1-7722	02: 24: 09.991	−04: 46: 7.83	$1.66^{+0.14}_{-0.13}$	11.50	$5.80^{+0.13}_{-0.13}$	$2.35^{+0.13}_{-0.12}$	$0.89^{+0.01}_{-0.01}$
ECDFS-36	03: 31: 54.522	−28: 02: 22.66	$1.74^{+0.08}_{-0.08}$	11.41	$10.27^{+0.00}_{-0.00}$	$0.42^{+0.00}_{-0.00}$	$0.49^{+0.00}_{-0.00}$
COSMOS-75358*	10: 02: 28.491	02: 02: 13.70	1.822^b	11.50	$3.36^{+0.23}_{-0.20}$	$3.68^{+0.35}_{-0.36}$	$0.73^{+0.17}_{-0.08}$
COSMOS-97596*	10: 02: 32.428	02: 22: 40.59	$1.84^{+0.13}_{-0.09}$	11.28	$7.55^{+1.26}_{-1.29}$	$3.46^{+0.45}_{-0.58}$	$0.46^{+0.10}_{-0.03}$
COSMOS-189978	10: 02: 14.418	02: 35: 11.92	$1.84^{+0.16}_{-0.14}$	11.50	$14.92^{+3.32}_{-3.74}$	$3.32^{+0.27}_{-0.30}$	$0.93^{+0.04}_{-0.03}$
ECDFS-4444*	03: 33: 11.482	−27: 49: 16.06	$1.87^{+0.16}_{-0.15}$	11.43	$3.25^{+0.10}_{-0.11}$	$4.82^{+0.36}_{-0.36}$	$0.84^{+0.06}_{-0.05}$
COSMOS-207160*	10: 00: 33.479	02: 28: 54.74	$1.90^{+0.13}_{-0.10}$	11.25	$6.71^{+1.93}_{-1.88}$	$8.00^{+0.00}_{-0.00}$	$0.58^{+0.24}_{-0.03}$
COSMOS-51726*	09: 59: 23.943	01: 44: 11.52	$1.94^{+0.05}_{-0.05}$	11.46	$4.62^{+0.04}_{-0.04}$	$2.64^{+0.12}_{-0.12}$	$0.92^{+0.27}_{-0.02}$
COSMOS-37208	09: 59: 42.594	01: 55: 01.55	$1.95^{+0.07}_{-0.07}$	11.54	$6.35^{+0.01}_{-0.01}$	$1.51^{+0.02}_{-0.02}$	$0.77^{+0.00}_{-0.00}$
CFHTD4-39098	22: 16: 52.676	−17: 26: 29.17	$1.99^{+0.15}_{-0.14}$	11.55	$3.95^{+0.06}_{-0.07}$	$4.09^{+0.33}_{-0.33}$	$0.89^{+0.01}_{-0.01}$
COSMOS-71932	10: 01: 40.598	01: 58: 57.47	$2.07^{+0.10}_{-0.11}$	11.70	$4.17^{+1.63}_{-1.06}$	$4.67^{+1.49}_{-1.14}$	$0.75^{+0.02}_{-0.02}$
COSMOS-103240	10: 00: 47.179	01: 59: 19.56	$2.09^{+0.09}_{-0.08}$	11.49	$28.0^{+4.19}_{-2.55}$	$8.00^{+0.00}_{-0.00}$	$0.60^{+0.01}_{-0.01}$
CFHTD1-26413	2: 26: 42.090	−04: 40: 39.88	$2.10^{+0.21}_{-0.21}$	11.50	$3.12^{+0.04}_{-0.04}$	$2.65^{+0.17}_{-0.17}$	$0.65^{+0.01}_{-0.01}$
COSMOS-230111	10: 01: 23.525	02: 45: 40.07	$2.45^{+0.17}_{-0.17}$	11.52	$10.53^{+15.5}_{-9.21}$	$2.72^{+2.14}_{-2.62}$	$0.75^{+0.10}_{-0.18}$
UDS-108509	02: 18: 46.503	−04: 59: 29.3	$2.56^{+0.08}_{-0.08}$	11.26	$3.42^{+0.02}_{-0.02}$	$1.73^{+0.06}_{-0.06}$	$0.64^{+0.01}_{-0.01}$
COSMOS-90679	10: 01: 57.001	02: 16: 12.14	$2.56^{+0.07}_{-0.07}$	11.63	$6.27^{+0.15}_{-0.15}$	$4.91^{+0.34}_{-0.34}$	$0.67^{+0.01}_{-0.01}$
UDS-90845	02: 17: 12.786	−05: 04: 49.97	$2.59^{+0.08}_{-0.08}$	11.41	$8.40^{+2.51}_{-1.46}$	$8.00^{+0.00}_{-0.00}$	$0.82^{+0.02}_{-0.02}$
UDS-46645	02: 16: 59.092	−05: 18: 07.07	$2.60^{+0.08}_{-0.08}$	11.41	$1.98^{+0.07}_{-0.07}$	$3.08^{+0.23}_{-0.23}$	$0.52^{+0.03}_{-0.03}$
UDS-97905	02: 16: 08.893	−05: 02: 37.69	$2.61^{+0.06}_{-0.06}$	11.29	$5.25^{+0.51}_{-0.61}$	$7.28^{+0.78}_{-0.82}$	$0.66^{+0.01}_{-0.01}$
UDS-35621*	02: 18: 19.404	−05: 21: 32.67	$2.64^{+0.11}_{-0.10}$	11.23	$6.14^{+1.61}_{-2.73}$	$5.94^{+0.98}_{-1.64}$	$0.74^{+0.17}_{-0.20}$
UDS-37091*	02: 17: 09.297	−05: 21: 07.42	$2.65^{+0.09}_{-0.08}$	11.16	$1.60^{+0.07}_{-0.07}$	$4.03^{+0.54}_{-0.54}$	$0.43^{+0.31}_{-0.01}$
COSMOS-53395	09: 58: 10.638	01: 45: 31.92	$2.67^{+0.25}_{-0.26}$	11.57	$4.34^{+0.14}_{-0.14}$	$0.69^{+0.03}_{-0.03}$	$0.77^{+0.01}_{-0.01}$
CFHTD1-29073	02: 26: 25.408	−04: 36: 5.42	$2.67^{+0.20}_{-0.19}$	11.71	$7.01^{+0.25}_{-0.25}$	$4.91^{+0.32}_{-0.32}$	$0.83^{+0.01}_{-0.01}$
CFHTD1-20942*	02: 26: 49.300	−04: 49: 20.53	$2.71^{+0.11}_{-0.11}$	11.70	$1.61^{+0.05}_{-0.05}$	$2.40^{+0.23}_{-0.23}$	$0.89^{+0.12}_{-0.05}$
UDS-138948	02: 17: 34.679	−04: 50: 09.92	$2.72^{+0.10}_{-0.10}$	11.39	$4.76^{+0.13}_{-0.13}$	$2.81^{+0.22}_{-0.22}$	$0.72^{+0.01}_{-0.01}$
CFHTD1-3114	02: 24: 29.921	−04: 52: 38.92	$2.80^{+0.08}_{-0.08}$	11.55	$1.36^{+0.08}_{-0.08}$	$7.42^{+1.00}_{-1.00}$	$0.63^{+0.04}_{-0.04}$
UDS-99096	02: 17: 09.861	−05: 02: 17.17	$2.84^{+0.14}_{-0.12}$	11.27	$9.13^{+7.4}_{-3.8}$	$8.00^{+0.00}_{-0.00}$	$0.96^{+0.03}_{-0.04}$
UDS-3433	02: 17: 56.693	−05: 31: 16.65	$2.90^{+0.15}_{-0.14}$	11.26	$32.5^{+11.7}_{-16.1}$	$6.54^{+0.77}_{-1.39}$	$0.70^{+0.01}_{-0.01}$
UDS-19400*	02: 19: 11.929	−05: 26: 24.62	$2.93^{+0.17}_{-0.21}$	11.18	$3.70^{+0.24}_{-0.27}$	$3.78^{+0.78}_{-0.79}$	$0.31^{+0.55}_{-0.04}$

Note. Properties of the $1.5 < z < 3$ massive galaxy sample selected for targeted imaging follow-up. Listed redshifts are $z_{\rm peak}$ values from modeling photometric catalogs; targets with available spectroscopic redshifts are indicated with superscripts (redshift source: ^{a} Hilton et al. 2010; ^{b} Onodera et al. 2012). ID's with * indicate targets that are resolved as multiple components/close pairs in *HST* H_{160} imaging. The listed stellar masses correspond to values from the parent catalogs for targets resolved as single objects in both ground and *HST* imaging, whereas for the targets resolved as multiple components it corresponds to the decomposed (catalog) stellar masses calculated in Section 3.2. Also listed are the best-fit GALFIT structural parameters (R_e, Sérsic index n and axis ratio b/a).

blue solid lines) for the corresponding redshift bins are plotted in each panel to aid the eye. We find that at $1.5 < z < 2.5$, the sizes of both star-forming and quiescent galaxies with $\log(M_*/M_\odot) > 11.2$ are relatively consistent with those found in van der Wel et al. (2014). At $2.5 < z < 3.0$, the sizes of the very massive star-forming galaxies ($\log(M_*/M_\odot) > 11.4$) appears to follow the extrapolation of the lower stellar-mass galaxy sizes. Interestingly, the mean sizes for quiescent galaxies at $\log(M_*/M_\odot) > 11.2$ appear to be systematically larger than what is expected based on the extrapolation of the relation derived from lower stellar mass galaxies, hinting to either a steeper size–stellar mass relation of quiescent galaxies, or at a break at $\log(M_*/M_\odot) \sim 11.2$, such that more massive

galaxies at $2.5 < z < 3$ have already reached their sizes, while the lower mass galaxies have yet to grow (see Patel et al. 2017).

4.2. Effect of Blending on the Massive End of SMF at $1.5 < z < 3$

To investigate the effect of blending on the high-mass end tail of the measured SMF, we estimated the "blending correction" factor necessary to the number density of observed galaxies to account for this effect. Specifically, we compared the number of galaxies in the *HST* sample before and after correcting for blending in redshift bins of $z = 1.5 - 2.5$, $2.5 - 3.0$ and in stellar mass bins of $\log(M_*/M_\odot) = 11.00 - 11.25$, $11.25 - 11.50$ and >11.50. We applied this factor to the volume density
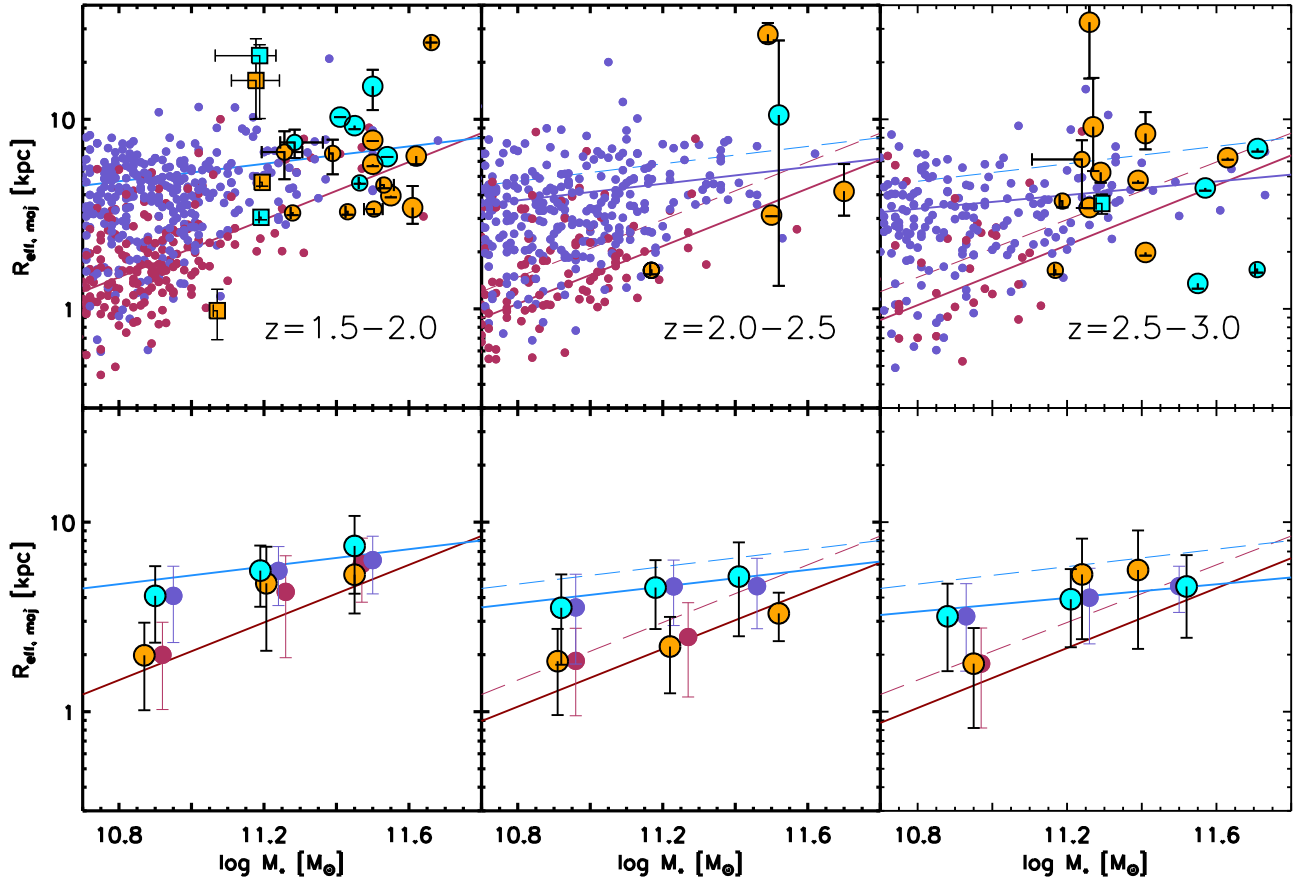
Figure 9. Size–stellar mass relation in three redshift ranges, namely $1.5 < z < 2.0$, $2.0 < z < 2.5$, and $2.5 < z < 3.0$. Filled orange and cyan circles represent our targeted sample of quiescent and star-forming galaxies, respectively. The smaller red and blue filled circles represents the quiescent and star-forming galaxies from van der Wel et al. (2014) using the CANDELS survey. Top panels show individual size measurements. The bottom panels show the biweighted mean sizes and dispersions for the van der Wel et al. (2014) sample (red and purple), and including our sample (orange and cyan). Also plotted are the size–stellar mass relations from van der Wel et al. (2014, red and blue solid lines). The $1.5 < z < 2.0$ relations are overplotted in the higher redshift panels as dashed curves.
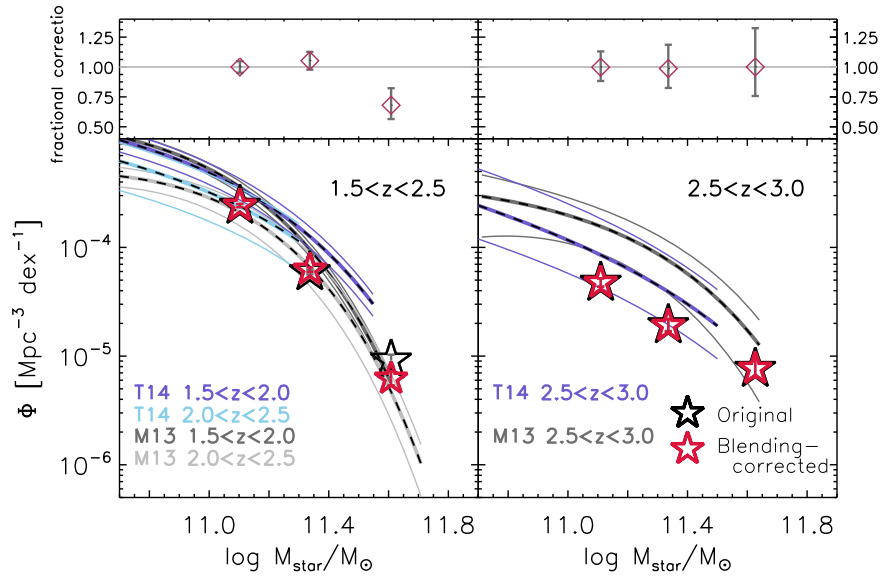

Figure 10. Lower panels: the stellar mass function, in stellar mass bins of $\Delta M_* = 0.25$ dex before (black stars) and after correcting for the effect of blended galaxies in the ground-based K band imaging (red stars). Also plotted are SMFs (thick curves with black dashes) from Muzzin et al. (2013a, light and dark gray curves) and Tomczak et al. (2014, blue and purple curves), and their total 1σ errors in the respective redshift bins (thin curves). Top panels: the fractional correction to account for close pairs on the SMF for the redshift and stellar mass bins considered (Φ_{corr}/Φ_{old}).
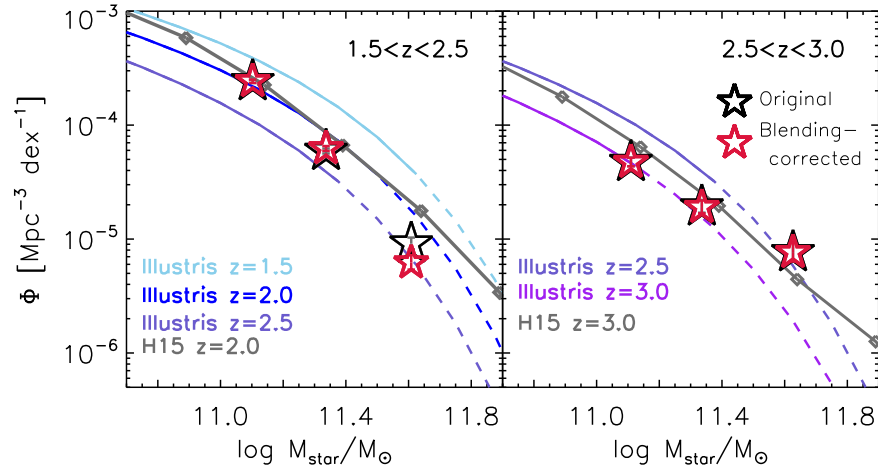
Figure 11. Stellar mass function, with star symbols identical to those in Figure 10. Gray curves represent the $z = 2$ and $z = 3.0$ stellar mass functions from the Munich galaxy formation model presented in Henriques et al. (2015). Blue solid curves indicate galaxy stellar mass functions from the Illustris cosmological hydrodynamical simulation (Torrey et al. 2015), calculated at the limiting redshifts for each panel ($z = 1.5, 2.0, 2.5, 3.0$ mass functions shown in light blue, blue, dark blue, and purple, respectively; dashed curves indicate the extrapolation of the mass function to $\Phi < 3 \times 10^{-5}$ Mpc^{-3}dex^{-1}).

of galaxies above the completeness limit for each survey and field in identical M_* and z bins. Again, we acknowledge that, lacking spectroscopic redshift identifications, it is impossible to thoroughly assess the difference in redshift and stellar populations for the individual galaxies discovered in close pairs, and hence calculate the *absolute* correction factors necessary to account for blending.

Figure 10 shows the calculated SMFs at $1.5 < z < 2.5$ and $2.5 < z < 3.0$ before (black stars) and after correcting (red stars) for the effect of galaxy blending in the ground-based K band imaging. Also overplotted are SMFs at the targeted redshifts from Muzzin et al. (2013a, light and dark gray curves) and Tomczak et al. (2014, blue and purple curves) in their probed stellar mass regimes. We find that at $2.5 < z < 3.0$, blending in ground-based K band imaging does not seem to significantly effect the extreme massive end ($\log(M_*/M_\odot) > 11$) of the SMF. However, at $1.5 < z < 2.5$, the effect of blending is substantial for the largest stellar mass bin considered, at the level of a factor ~ 1.5. We note that the blending-corrected results are consistent with the SMFs of Muzzin et al. (2013a).

Figure 11 shows the same calculated number densities as Figure 10, this time compared with the predictions from theoretical studies. The gray solid curve in each redshift panel represents the galaxy SMF from the updated Munich galaxy formation model of Henriques et al. (2015; with stellar masses shifted by $+0.14$ dex to convert from Maraston 2005 to Bruzual & Charlot 2003 stellar populations), calculated based on the Millennium (Springel et al. 2005) and Millennium-II (Boylan-Kolchin et al. 2009) dark matter simulations updated to *Planck* first-year cosmology. Also shown in each panel are the fits to the (differential) galaxy SMF from the cosmological hydrodynamical simulation Illustris (Torrey et al. 2015), calculated at the limits of each redshift bin. The Illustris SMFs at $z = 1.5, 2.0, 2.5, 3.0$ are shown in light blue, blue, dark blue, and purple solid curves, respectively, for the valid range indicated in that study ($\Phi > 3 \times 10^{-5}$Mpc^{-3}dex^{-1}; the extrapolation of the fit to lower mass function values is indicated by dashed curves).>

We find that the predicted SMFs presented in Torrey et al. (2015) for galaxies at $1.5 < z < 3.0$ are consistent with

observations within the valid parameter space of Illustris. The volume probed by Illustris limits inferring predictions for the mass function at the extreme massive end of the galaxy population due to the rarity of these objects, which corresponds to a lower limit on the value of the SMF ($\Phi = 3 \times 10^{-5}$ Mpc^{-3} dex^{-1}, corresponding to $\log(M_*/M_\odot) \sim 11.6$ and 11.1 at $z \approx 1.5$ and 3.0, respectively). We highlight the large volumes necessary to make predictions for the extraordinary, ultra-massive galaxies at $z > 1.5$. Specifically, the next generation of hydrodynamical simulations such as ILLUSTRISTNG (Pillepich et al. 2018) is necessary to infer the behavior of the SMF at the extreme massive end of galaxy populations.

As expected from the larger volumes of SAMs, predictions from Henriques et al. (2015) probe the SMF to larger stellar masses. In the low redshift bin ($1.5 < z < 2.5$), Henriques et al. (2015) overpredicts the abundance of galaxies. We note that this is also the stellar mass bin where galaxy blending most significantly affects the inferred number density of galaxies, increasing the tension between theoretical predictions and observations. The discrepancy between Henriques et al. (2015) predictions and our observations is more evident in the higher redshift bin ($2.5 < z < 3.0$), where the SMF is underestimated for galaxies at $\log(M_*/M_\odot) > 11.4$. In contrast to the trend observed at $z < 2.5$, the effect of galaxy blending works to bring the observed SMF more in line with theoretical predictions, although the estimated correction for blending is negligible in this redshift bin. However, we note that the remaining disagreement is not significant after accounting for uncertainties due to SED-modeling assumptions (a potential factor of ~ 2, i.e., ~ 0.3 dex in stellar mass). This makes it clear that deriving accurate M_*/L_H ratios, and hence stellar masses for these targets is necessary through detailed spectroscopic analyses.

Finally, we stress that this early investigation of the effects of blending on the inferred number densities of very massive galaxies at high redshift serves to illustrate that this is an additional avenue to rein in on the systematic uncertainties related to observationally characterizing this population. More to the point, we caution that the inferred correction factors should not be blindly applied to different data sets.

5. Discussion and Summary

We presented the investigation of the structural properties of very massive galaxies ($\log(M_*/M_\odot) > 11.25$) at $1.5 < z_{phot} < 3.0$. Owing to their low spatial density in the distant universe, identifying and assembling a large enough sample of very massive galaxies requires large survey volumes. We selected a sample of 37 galaxies from the combined UltraVISTA, NMBS-II, and UDS catalogs to perform *HST* WFC3/F160W follow-up imaging in order to accurately determine their sizes and morphologies. We modeled their 2D light profiles using GALFIT and compared their size distributions with the high-z sample of van der Wel et al. (2014). Visual investigation of the H_{160} imaging revealed that 13/37 targets were unresolved in the parent K band catalogs. We investigated the effect of galaxy blending on the SMF at $1.5 < z < 3.0$ by decomposing the estimated stellar masses of the close-pair systems based on their observed H_{160} fluxes. It is important to note that, lacking spectroscopic redshift identifications, we cannot fully determine the stellar populations of individual galaxies identified in close pairs, and hence conclusively assess the effect of blending on the stellar masses. Based on this analysis the results can be summarized as follows:

1. At $1.5 < z < 2.5$, the sizes of both star-forming and quiescent galaxies with $\log(M_*/M_\odot) > 11.2$ are relatively consistent with those found in van der Wel et al. (2014).
2. At $2.5 < z < 3$, sizes for quiescent galaxies at $\log(M_*/M_\odot) > 11.2$ appear to be systematically larger than what is expected based on the extrapolation of the relation derived from lower stellar mass galaxies, confirming results in Patel et al. (2017).
3. We found that the effect of galaxy blending is most significant for the largest stellar mass bin ($\log(M_*/M_\odot) \approx 11.6$) considered at $1.5 < z < 2.5$, although it remains consistent with the SMF of Muzzin et al. (2013b, as calculated from the maximum likelihood method).
4. From the comparison with theoretical predictions, we find that the Illustris simulation agrees well with the observed number density, although their simulated volume is too small to probe the most massive galaxies. Similarly good agreement at $\log(M_*/M_\odot) < 11.5$ is found between observations and the predictions from the SAM of Henriques et al. (2015). However, the observed number density of the most massive galaxies (i.e., $\log(M_*/M_\odot) > 11.5$) is overpredicted at $1.5 < z < 2.5$ and underpredicted at $2.5 < z < 3.0$.

Facility: HST(WFC3).

Appendix
Observed Spectral Energy Distributions and p(z) of Targets

The observed SEDs and the redshift probability distributions for the targets in this sample are displayed in Figures 12–14. The SEDs are well sampled with the available medium- and broadband photometry, and a strong rest-frame optical break is evident in all targets, indicative of relatively evolved stellar populations.
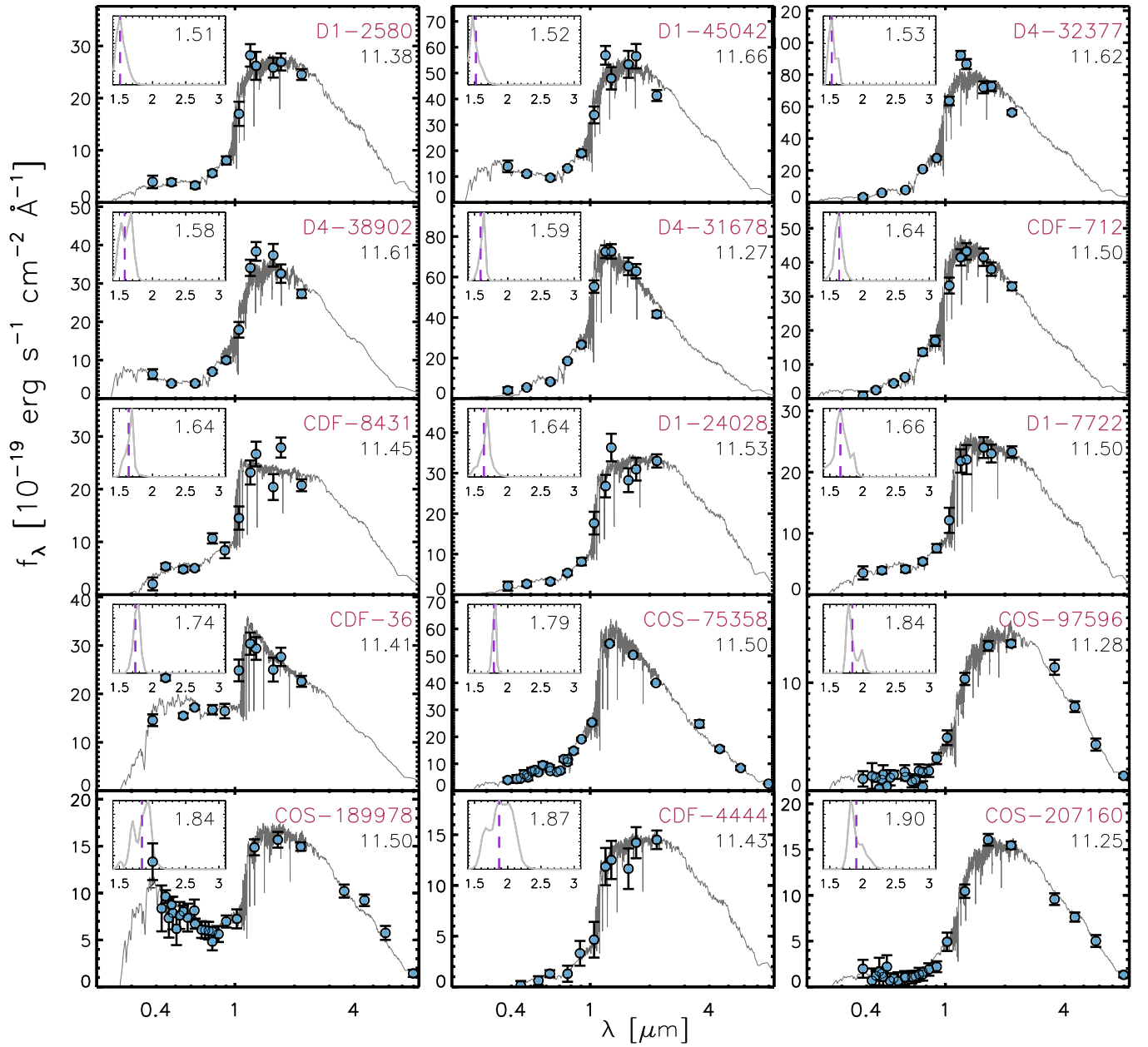
Figure 12. Observed UV-IR spectral energy distributions for the massive galaxies at $1.5 < z < 3$ selected for targeted follow-up observations using *HST/WFC3 H_{160}*. Photometry from parent catalogs are shown by blue filled symbols, in units of 10^{-19} erg cm^{-2} s^{-1} Å^{-1} and the gray curves represent the best-fit *FAST* templates. The insets display the redshift probability distribution ($p(z)$) for each target. The ID, z_{phot} and stellar mass ($\log(M_*/M_\odot)$) of targets are listed in each panel, using the abbreviations COS, D1, D4, and CDF to denote targets in the COSMOS, CFHTD-1, CFHTD-4, and ECDFS fields, respectively.
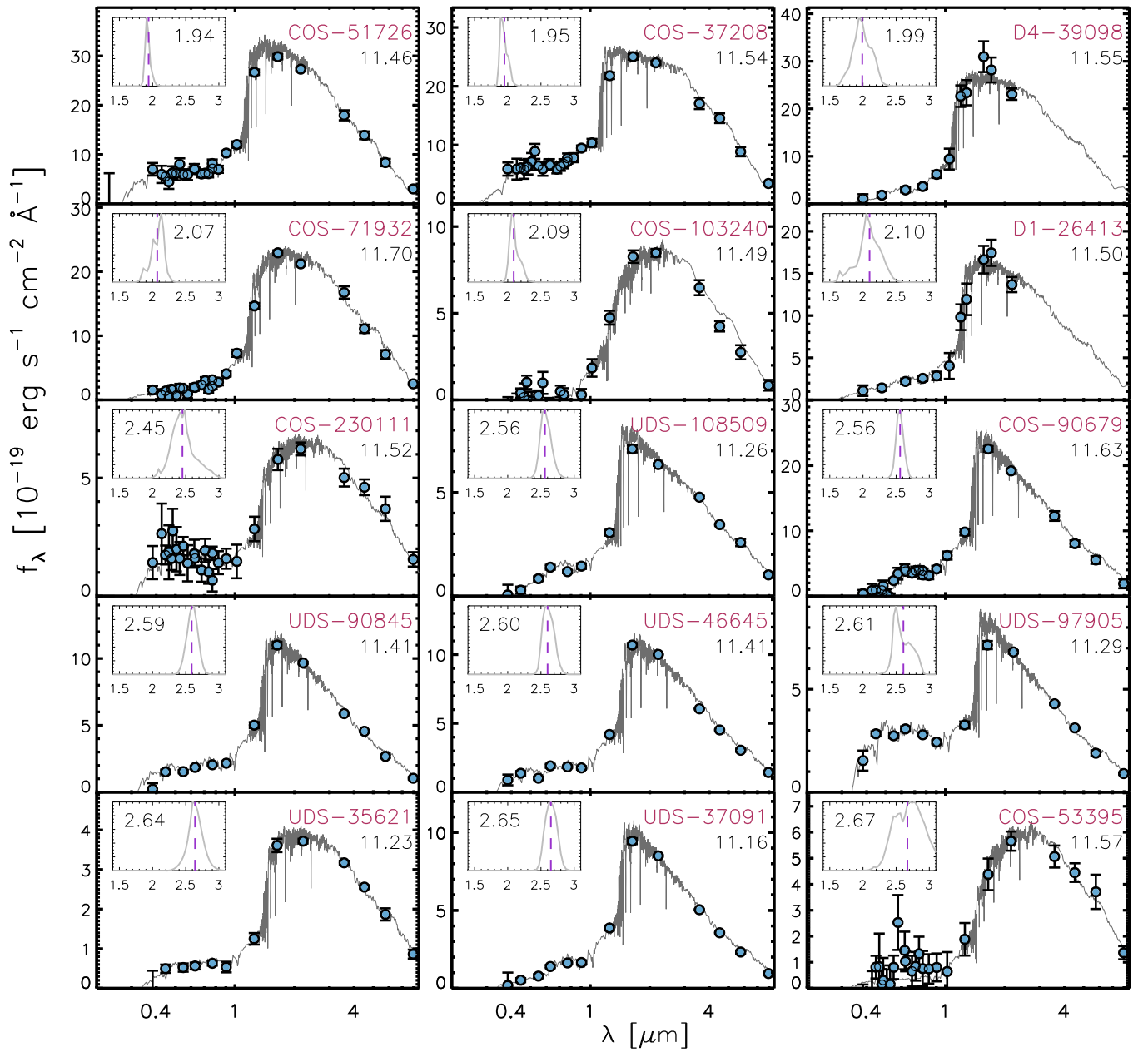
Figure 13. Observed UV-IR spectral energy distributions for the massive galaxies at $1.5 < z < 3$ selected for targeted follow-up observations using *HST/WFC3 H_{160}*. Photometry from parent catalogs are shown by blue filled symbols, in units of 10^{-19} erg cm^{-2} s^{-1} Å^{-1} and the gray curves represent the best-fit FAST templates. The insets display the redshift probability distribution ($p(z)$) for each target. The ID, z_{phot}, and stellar mass ($\log(M_*/M_\odot)$) of targets are listed in each panel, using the abbreviations COS, D1, D4, and CDF to denote targets in the COSMOS, CFHTD-1, CFHTD-4, and ECDFS fields, respectively.
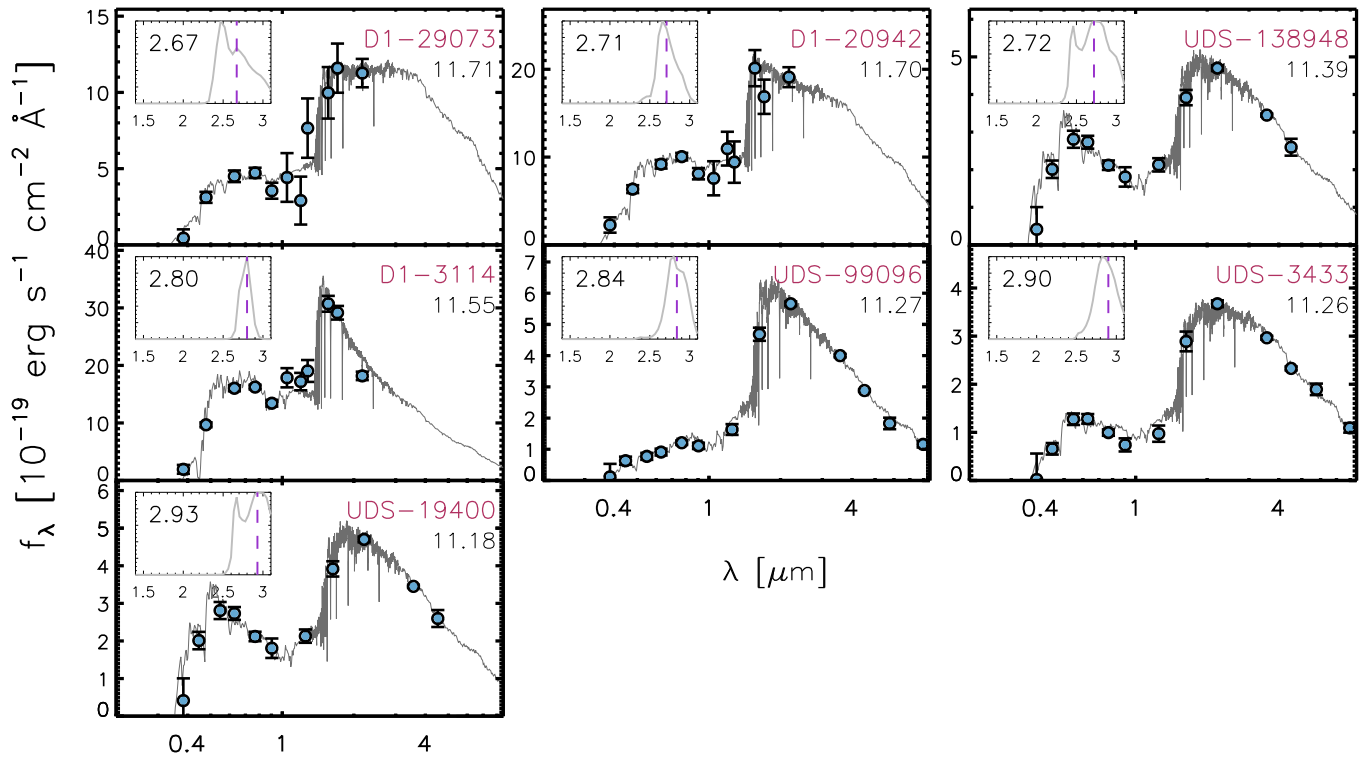
Figure 14. Observed UV-IR spectral energy distributions for the massive galaxies at $1.5 < z < 3$ selected for targeted follow-up observations using *HST/WFC3 H*$_{160}$. Photometry from parent catalogs are shown by blue filled symbols, in units of 10^{-19} erg cm^{-2} s^{-1} Å^{-1} and the gray curves represent the best-fit FAST templates. The insets display the redshift probability distribution ($p(z)$) for each target. The ID, z_{phot}, and stellar mass ($\log(M_*/M_\odot)$) of targets are listed in each panel, using the abbreviations COS, D1, D4, and CDF to denote targets in the COSMOS, CFHTD-1, CFHTD-4, and ECDFS fields, respectively.

ORCID iDs

Z. Cemile Marsan ⓘ https://orcid.org/0000-0002-7248-1566
Danilo Marchesini ⓘ https://orcid.org/0000-0001-9002-3502
Adam Muzzin ⓘ https://orcid.org/0000-0002-9330-9108
Gabriel B. Brammer ⓘ https://orcid.org/0000-0003-2680-005X
Rachel Bezanson ⓘ https://orcid.org/0000-0001-5063-8254
Marijn Franx ⓘ https://orcid.org/0000-0002-8871-3026
Britt Lundgren ⓘ https://orcid.org/0000-0002-6463-2483
Gregory Rudnick ⓘ https://orcid.org/0000-0001-5851-1856
Mauro Stefanon ⓘ https://orcid.org/0000-0001-7768-5309
Pieter van Dokkum ⓘ https://orcid.org/0000-0002-8282-9888
David Wake ⓘ https://orcid.org/0000-0002-6047-1010
Katherine E. Whitaker ⓘ https://orcid.org/0000-0001-7160-3632

References

Allen, R. J., Kacprzak, G. G., Glazebrook, K., et al. 2017, ApJL, 834, L11
Annunziatella, M., Marchesini, D., Stefanon, M., et al. 2018, PASP, 130, 124501
Belli, S., Newman, A. B., & Ellis, R. S. 2014, ApJ, 783, 117
Belli, S., Newman, A. B., & Ellis, R. S. 2015, ApJ, 799, 206
Bernardi, M., Sheth, R. K., Annis, J., et al. 2003, AJ, 125, 1882
Bezanson, R., van Dokkum, P. G., Tal, T., et al. 2009, ApJ, 697, 1290
Bournaud, F. 2016, in Astrophysics and Space Science Library Vol. 418, Galactic Bulges, ed. E. Laurikainen, R. Peletier, & D. Gadotti (Berlin: Springer), 355
Boylan-Kolchin, M., Springel, V., White, S. D. M., Jenkins, A., & Lemson, G. 2009, MNRAS, 398, 1150
Brammer, G. B., van Dokkum, P. G., & Coppi, P. 2008, ApJ, 686, 1503
Bruzual, G., & Charlot, S. 2003, MNRAS, 344, 1000
Buitrago, F., Trujillo, I., Conselice, C. J., et al. 2008, ApJL, 687, L61
Buitrago, F., Trujillo, I., Curtis-Lake, E., et al. 2017, MNRAS, 466, 4888
Calzetti, D., Armus, L., Bohlin, R. C., et al. 2000, ApJ, 533, 682
Caputi, K. I., Ilbert, O., Laigle, C., et al. 2015, ApJ, 810, 73

Chabrier, G. 2003, ApJL, 586, L133
Cimatti, A., Cassata, P., Pozzetti, L., et al. 2008, A&A, 482, 21
Damjanov, I., McCarthy, P. J., Abraham, R. G., et al. 2009, ApJ, 695, 101
Davidzon, I., Ilbert, O., Laigle, C., et al. 2017, A&A, 605, A70
Dekel, A., & Burkert, A. 2014, MNRAS, 438, 1870
Dekel, A., Sari, R., & Ceverino, D. 2009, ApJ, 703, 785
Duncan, K., Conselice, C. J., Mortlock, A., et al. 2014, MNRAS, 444, 2960
Faisst, A. L., Carollo, C. M., Capak, P. L., et al. 2017, ApJ, 839, 71
Franx, M., van Dokkum, P. G., Förster Schreiber, N. M., et al. 2008, ApJ, 688, 770
Furlong, M., Bower, R. G., Crain, R. A., et al. 2017, MNRAS, 465, 722
Gallazzi, A., Charlot, S., Brinchmann, J., & White, S. D. M. 2006, MNRAS, 370, 1106
Gallazzi, A., Charlot, S., Brinchmann, J., White, S. D. M., & Tremonti, C. A. 2005, MNRAS, 362, 41
Genel, S., Nelson, D., Pillepich, A., et al. 2018, MNRAS, 474, 3976
Glazebrook, K., Schreiber, C., Labbé, I., et al. 2017, Natur, 544, 71
Grazian, A., Fontana, A., Santini, P., et al. 2015, A&A, 575, A96
Hasinger, G., Capak, P., Salvato, M., et al. 2018, ApJ, 858, 77
Henriques, B. M. B., White, S. D. M., Thomas, P. A., et al. 2015, MNRAS, 451, 2663
Hill, A. R., Muzzin, A., Franx, M., et al. 2017, ApJ, 837, 147
Hilton, M., Lloyd-Davies, E., Stanford, S. A., et al. 2010, ApJ, 718, 133
Hilz, M., Naab, T., Ostriker, J. P., et al. 2012, MNRAS, 425, 3119
Hilz, M., Naab, T., & Ostriker, J. P. 2013, MNRAS, 429, 2924
Hopkins, P. F., Hernquist, L., Cox, T. J., et al. 2006, ApJS, 163, 1
Huang, S., Leauthaud, A., Greene, J., et al. 2018a, MNRAS, 480, 521
Huang, S., Leauthaud, A., Greene, J. E., et al. 2018b, MNRAS, 475, 3348
Ilbert, O., McCracken, H. J., Le Fèvre, O., et al. 2013, A&A, 556, A55
Khochfar, S., & Silk, J. 2006, MNRAS, 370, 902
Koekemoer, A. M., Faber, S. M., Ferguson, H. C., et al. 2011, ApJS, 197, 36
Kriek, M., van Dokkum, P. G., Franx, M., Illingworth, G. D., & Magee, D. K. 2009a, ApJL, 705, L71
Kriek, M., van Dokkum, P. G., Labbé, I., et al. 2009b, ApJ, 700, 221
Krumholz, M., & Burkert, A. 2010, ApJ, 724, 895
Kuntschner, H., Emsellem, E., Bacon, R., et al. 2010, MNRAS, 408, 97
Labbé, I., Huang, J., Franx, M., et al. 2005, ApJL, 624, L81
Lawrence, A., Warren, S. J., Almaini, O., et al. 2007, MNRAS, 379, 1599

Le Fèvre, O., Tasca, L. A. M., Cassata, P., et al. 2015, A&A, 576, A79
Lilly, S. J., Le Fèvre, O., Renzini, A., et al. 2007, ApJS, 172, 70
Maraston, C. 2005, MNRAS, 362, 799
Marchesini, D., Whitaker, K. E., Brammer, G., et al. 2010, ApJ, 725, 1277
Marsan, Z. C., Marchesini, D., Brammer, G. B., et al. 2015, ApJ, 801, 133
Marsan, Z. C., Marchesini, D., Brammer, G. B., et al. 2017, ApJ, 842, 21
Martis, N. S., Marchesini, D., Brammer, G. B., et al. 2016, ApJL, 827, L25
McCracken, H. J., Milvang-Jensen, B., Dunlop, J., et al. 2012, A&A, 544, A156
McDermid, R. M., Alatalo, K., Blitz, L., et al. 2015, MNRAS, 448, 3484
McLure, R. J., Pentericci, L., Cimatti, A., et al. 2018, MNRAS, 479, 25
Momcheva, I. G., Brammer, G. B., van Dokkum, P. G., et al. 2016, ApJS, 225, 27
Muzzin, A., Marchesini, D., Stefanon, M., et al. 2013a, ApJS, 206, 8
Muzzin, A., Marchesini, D., Stefanon, M., et al. 2013b, ApJ, 777, 18
Naab, T., Johansson, P. H., & Ostriker, J. P. 2009, ApJL, 699, L178
Newman, A. B., Ellis, R. S., Bundy, K., & Treu, T. 2012, ApJ, 746, 162
Nipoti, C., Londrillo, P., & Ciotti, L. 2003, MNRAS, 342, 501
Onodera, M., Renzini, A., Carollo, M., et al. 2012, ApJ, 755, 26
Oser, L., Ostriker, J. P., Naab, T., Johansson, P. H., & Burkert, A. 2010, ApJ, 725, 2312
Patel, S. G., Fumagalli, M., Franx, M., et al. 2013, ApJ, 778, 115
Patel, S. G., Hong, Y. X., Quadri, R. F., Holden, B. P., & Williams, R. J. 2017, ApJ, 839, 127
Peng, C. Y., Ho, L. C., Impey, C. D., & Rix, H.-W. 2002, AJ, 124, 266
Pillepich, A., Springel, V., Nelson, D., et al. 2018, MNRAS, 473, 4077
Quadri, R. F., Williams, R. J., Franx, M., & Hildebrandt, H. 2012, ApJ, 744, 88
Schreiber, C., Glazebrook, K., Nanayakkara, T., et al. 2018, A&A, 618, 85
Scoville, N., Aussel, H., Brusa, M., et al. 2007, ApJS, 172, 1
Shen, S., Mo, H. J., White, S. D. M., et al. 2003, MNRAS, 343, 978
Song, M., Finkelstein, S. L., Ashby, M. L. N., et al. 2016, ApJ, 825, 5
Springel, V., White, S. D. M., Jenkins, A., et al. 2005, Natur, 435, 629
Straatman, C. M. S., Labbé, I., Spitler, L. R., et al. 2014, ApJL, 783, L14
Straatman, C. M. S., Labbé, I., Spitler, L. R., et al. 2015, ApJL, 808, L29
Szomoru, D., Franx, M., & van Dokkum, P. G. 2012, ApJ, 749, 121
Tasca, L. A. M., Le Fèvre, O., Ribeiro, B., et al. 2017, A&A, 600, A110
Terlevich, A. I., Caldwell, N., & Bower, R. G. 2001, MNRAS, 326, 1547
Thomas, D., Maraston, C., Bender, R., & Mendes de Oliveira, C. 2005, ApJ, 621, 673
Tomczak, A. R., Quadri, R. F., Tran, K.-V. H., et al. 2014, ApJ, 783, 85
Torrey, P., Wellons, S., Machado, F., et al. 2015, MNRAS, 454, 2770
Trager, S. C., Faber, S. M., Worthey, G., & González, J. J. 2000, AJ, 119, 1645
Trujillo, I., Feulner, G., Goranova, Y., et al. 2006, MNRAS, 373, L36
Trujillo, I., Rudnick, G., Rix, H.-W., et al. 2004, ApJ, 604, 521
van der Wel, A., Franx, M., van Dokkum, P. G., et al. 2014, ApJ, 788, 28
van der Wel, A., Rix, H.-W., Wuyts, S., et al. 2011, ApJ, 730, 38
van Dokkum, P. G., Bezanson, R., van der Wel, A., et al. 2014, ApJ, 791, 45
van Dokkum, P. G., Franx, M., Kriek, M., et al. 2008, ApJL, 677, L5
van Dokkum, P. G., Whitaker, K. E., Brammer, G., et al. 2010, ApJ, 709, 1018
Wellons, S., Torrey, P., Ma, C.-P., et al. 2015, MNRAS, 449, 361
Whitaker, K. E., Kriek, M., van Dokkum, P. G., et al. 2012, ApJ, 745, 179
Whitaker, K. E., Labbé, I., van Dokkum, P. G., et al. 2011, ApJ, 735, 86
Williams, R. J., Quadri, R. F., Franx, M., et al. 2010, ApJ, 713, 738
Williams, R. J., Quadri, R. F., Franx, M., van Dokkum, P., & Labbé, I. 2009, ApJ, 691, 1879
Yamada, Y., Arimoto, N., Vazdekis, A., & Peletier, R. F. 2006, ApJ, 637, 200